Control of the length of $Fe_{73.5}Si_{13.5}Nb_3Cu_1B_9$ microwires to be used for magnetic and microwave absorbing purposes

Papa Gorgui Birame Gueye[a,b], Jesús López Sánchez[b], Elena Navarro[a,b], Aída Serrano[c], and Pilar Marín[a,b]*

[a] Departamento de Física de Materiales, Universidad Complutense de Madrid, 28040 Madrid, Spain
[b] Instituto de Magnetismo Aplicado CSIC-ADIF, P.O. Box 155, Las Rozas, Madrid 28230, Spain
[c] Departamento de Electrocerámica, Instituto de Cerámica y Vidrio (ICV), CSIC, 28049 Madrid, Spain

*Corresponding author: jesus.lopez@ucm.es

KEYWORDS: microwave absorbing composites, tunable magnetic properties, multifunctional microwires, ball milling, filtering/sedimentation optimization processes, FeSiNbCuB microwires

Abstract

A combination of high energy ball milling, vacuum filtering and sedimentation processes has been demonstrated to be a useful approach to reduce, in a controlled way, the length of as-cast $Fe_{73.5}Si_{13.5}Nb_3Cu_1B_9$ amorphous magnetic microwires (MWs) and annealed material at 550 ºC in nitrogen condidions. Homogeneous compositional microstructures with fairly narrow size distributions between 1300 µm and 11.7 µm are achieved exhibiting tunable response as a soft magnetic material and as a microwave absorber. From the magnetic perspective, the soft magnetic character is increased with smaller length of the MWs whereas the remanence has the opposite behavior mainly due to the structural defects and the loss of the shape anisotropy. From the microwave absorption perspective, a novel potential applicability is tested in these refined microstructures. This innovation consists of coatings based on commercial paints with a filling percentage of 0.55% of MWs with different lengths deposited on metallic sheets. Large attenuation values around -40 dB are obtained in narrow spectral windows located in the GHz range and their position can be varied by combining different optimized lengths of MW. As an example of this powerful mechanism for absorbing microwaves at specific frequencies, MW lengths of 2 mm and 50 µm are chosen, where a precise tailoring of the minimum reflection loss (R_L) is obtained in a range between 8.85 GHz and 13.25 GHz. To confirm these experimental results an effective medium standard model proposed for electrical permittivity is used. Experimental and theoretical results are consistent and these novel composites are also proposed as a feasible candidate for designing frequency selective microwave absorbers on demand, with low filling percentages and high absorption intensity values.

1. Introduction:

$Fe_{73.5}Si_{13.5}Nb_3Cu_1B_9$ amorphous magnetic microwires (MWs) is probably the most studied soft magnetic material due to its interesting physical properties. It presents a high industrial upscaling and its technological applications are encompassed in multidisciplinary fields of investigation [1]. Magnetic sensors [2], biomedicine [3], electromagnetic attenuation [4], spintronics [5], magnetic hyperthermia [6] and magnetocaloric effects [7] are representative examples of its huge versatility [8]. These microstructures are continuous filaments with a soft magnetic nucleus covered by a glassy outer shell. Typically, the total diameter (D_{total}) is less than 100 μm and the metallic core diameter (D_{core}) is between 4 and 60 μm. Obtained by the Taylor-Ulitosky technique [9,10], the interesting properties of this material are mainly related to its amorphous character and the strong shape anisotropy supported by the glassy outer shell at the microscale [10]. Fine-control in its composition and its ratio between D_{total} and D_{core} [11] promotes changes in the magnetoelastic anisotropy and this is the origin of other potential technological properties as magnetic bistability [12], giant magnetoimpedance (GMI) [13,14], magnetoelastic effects [15] or natural ferromagnetic resonance (NFMR) [4,16].

The attractiveness of these amorphous MWs is enhanced further by their ability to transform into an ultra-soft magnetic material by promoting partial nanocrystallization processes with temperature [17,18]. To observe this effect, a thermal treatment performed at 550 ºC in nitrogen atmosphere is one of the most suitable procedures [3]. After annealing, α-Fe_3Si nanocrystals are formed with crystal domain sizes of 10-15 nm and the final microstructure shows a remarkable low coercivity ~1 Oe due to the influence of Cu, Nb and B atoms [4]. This partial nanocrystallized state favors the brittleness character instead of the amorphous one [19] and could be a good strategy to achieve the tuning of the MW physical properties on demand.

Focusing on this desirable point, the main objective of this investigation is to tailor the multifunctional features of amorphous and annealed $Fe_{73.5}Si_{13.5}B_9Cu_1Nb_3$ MWs by controlling their lengths. The strategy proposed in this work is based on a combination of high energy ball milling, vacuum filtration and sedimentation processes. The refined microstructures have a homogeneous morphological distribution and a correlated dependence on the shape anisotropy and the structural modifications created during the ball milling. As a consequence, unusual low frequency magnetic behaviors are identified such as a coercivity decrease at smaller length sizes.

On the other hand, a civil and military concern arises with the electromagnetic wave pollution as a result of the development of information technologies. An effective approach to solve this

problem in the GHz range is the use of microwave absorbing or interference shielding materials [19–22]. The absorption capacity of the waves depends on the combination between electrical and magnetic losses [8] and a good microwave absorbing material should fulfill the requirements of high reflection loss coefficient (R_L), and being lightweight and of low thickness. To this end, a wide variety of investigations have focused on carbon-based materials, ceramic materials, magnetic nanomaterials and other compounds [23–25]. In addition, innovative composites are designed taking into account the nanostructuring of the materials and the changes in the physical properties of one of their constituents that influence the overall behavior of the composite. Some examples of composite manufacturing engineering are Fe_3O_4/Graphene structures [26], laminated MXene/Ni composites [27], peapod-like MnO/C nanowires [28], NiO nanorings/SiC [29], and/or GeP nanosheets/paraffin wax [30]. However, considering real applications of these materials, it is still a challenge to design a highly effective, lightweight and stable materials with matching thickness below 1 mm and reflection losses below -30 dB.

In a previous study, our investigations revealed the possibility of developing composites consisting of commercial paints doped with $Fe_{89}Si_3B_1C_3Mn_4$ MWs for microwave attenuation with a minimum R_L of -30 dB in the X-band in a metal back-panel system [19,22]. Those composites fulfill the conditions to work as a radar absorbing materials and the high frequency absorbing properties depend mainly on their dielectric permittivity, magnetic permeability and sample thickness for impedance matching [4,8,22,31]. Following this line of research, a tuning of the attenuation in the radar absorption window is proposed by optimizing the length of the $Fe_{73.5}Si_{13.5}Nb_3Cu_1B_9$ MWs outlined above exploiting its multifunctionality. For this, composites based on commercial paints with selected length MWs are manufactured with volume fractions below the percolation threshold (p_c). The variation of the MW length modifies the effective permittivity of the composite (ε_{eff}) through its depolarization factor (N_z). When the MWs are shorter, the ε_{eff} decreases and the minimum R_L coefficient blueshifts to higher absorption frequency [4,22]. This approach therefore becomes as a powerful tool to select different absorption bands without varying the thickness of the composite.

The applicability of this concept is further tested by an effective medium standard model (Maxwell-Garnett approximation) proposed for electrical permittivity [32–34]. This model predicts the positions of the minimum R_L considering the physical characteristics of the MWs (inclusions) embedded in a dielectric matrix (host) and evaluates the impedance matching that influences the resulting ε_{eff} of the composite. The high consistency of these results opens a large

field of experimentation easily transferable to the industry and these composites are proposed as novel and efficient frequency selective microwave absorbers.

2. Experimental techniques:

2.1. High energy ball milling of amorphous and nanocrystalline magnetic MWs:

The schematic diagram of manufacturing and length optimization processes for annealed MWs is shown in Figure 1. Firstly, $Fe_{73.5}Si_{13.5}B_9Cu_1Nb_3$ alloy based on amorphous pyrex(borosilicate glass)-coated MWs, with a metal nucleus diameter of 9.4 μm and a total diameter of 20.2 μm is obtained by the rapid quenching Taylor-Ulitosky technique (step i) [9,10]. Subsequently, MWs are cut to 2 mm and annealed in a tubular furnace to obtain a α-Fe_3Si partial nanocrystallization at 550 ºC-1h in nitrogen atmosphere (step ii). As-cast MWs are cut to 2 mm of length and no annealing process was followed. In the step iii, as-cast and nanocrystallized MWs with 2 mm of length are subjected to a dry ball milling process from 2 to 10 min at a rotational speed of 1500 rpm to reduce their lengths. After the dry ball milling of both materials separately, the pyrex coating is removed by applying a Nd-Fe-B-based magnet to the resulting material (step iv). The obtained magnetic microstructures have a large size distribution, which is reduced by a vacuum filtering process using membranes with a porosity of ~20 μm and a subsequent sedimentation processes to discretize the length of the MWs (steps v and vi). During the sedimentation process, the microstructures with large length size distribution are added to a solution of absolute ethanol and ultrasonically sonicated for 15 min. Afterwards, the final solution is settle for 4 h. During this period of time, larger microstructures are gradually sedimentated while smaller microstructures float at the top of the solution [35]. From here, three different sizes are selected from settled-down (large-L), intermediate (medium-M) and floating-up (small-S) regions (Figure 1). This process is repeated for several times to get large and homogeneous quantities of the selected MW lenghts.

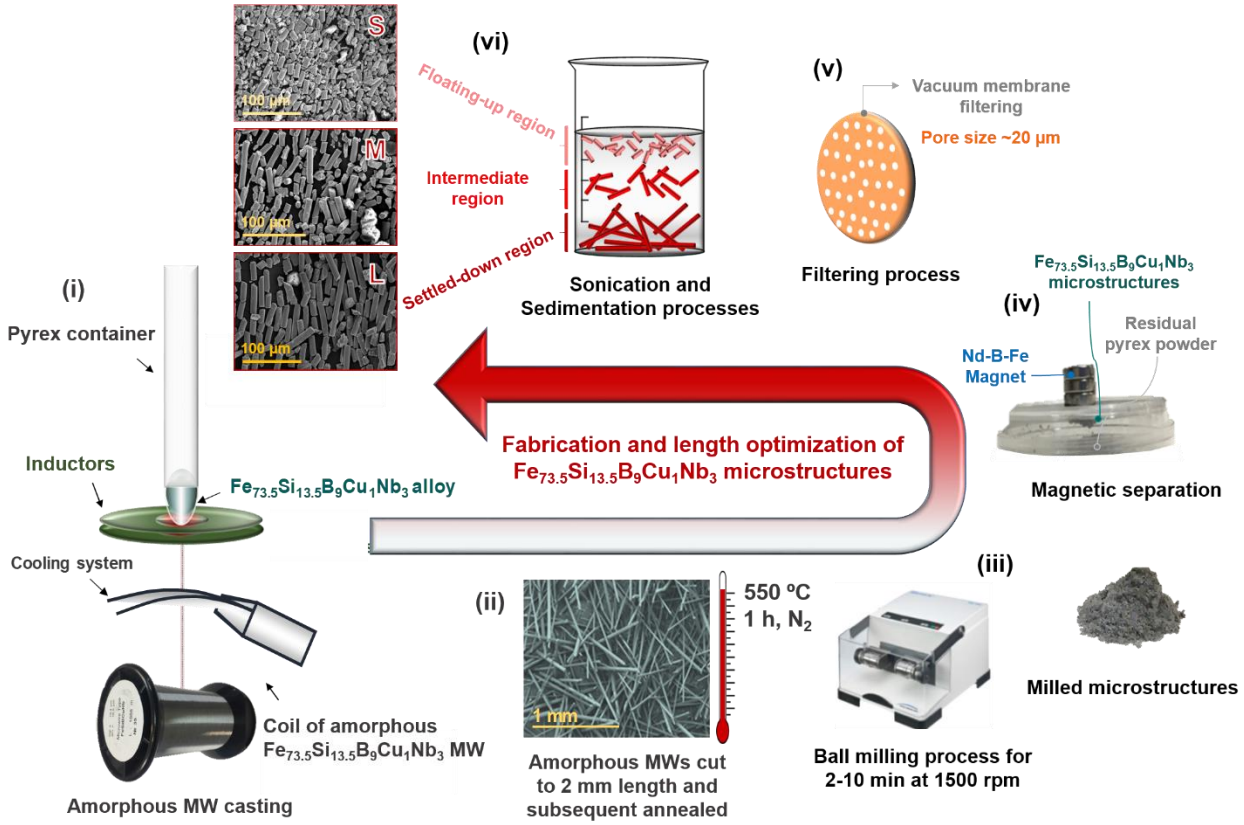

Figure 1. Schematic diagram of fabrication and length optimization processes to obtain the final annealed $Fe_{73.5}Si_{13.5}B_9Cu_1Nb_3$ MWs. (i) Fabrication process by rapid quenching Taylor-Ulitosky technique [9,10]; (ii) Cutting process to obtain 2 mm of length and subsequent annealing carried out at 550 ºC in N_2 atmosphere for 1 h; (iii) High energy ball milling at 1500 rpm from 2 to 10 min; (iv) Magnetic separation performed by approaching a Nd-B-Fe-based magnet; (v) Vacuum membrane filtering process; (vi) Sonication for 15 min and sedimentation for 4 h to obtain the length optimization of MWs (L, M and S regions). Similar procedure skipping the annealing process (step (ii)) was followed for as-cast amorphous MWs.

2.2.Microstructural and low frequency magnetic characterization:

Morphological aspects and structural properties of the milled microstructures are examined by scanning electron microscopy (SEM) images using a JEOL JSM 6400 apparatus. The crystal structure and composition of samples are studied by X-ray diffraction (XRD), using a PANalytical X'Pert MPD system with Cu Kα radiation (λ = 1.542 Å). X-ray absorption spectroscopy (XAS) measurements at the Fe K-edge are performed at the CRG-BM25A SpLine beamline in The European Synchrotron (ESRF), Grenoble (France). XAS data are collected in transmission mode at room temperature, with a total of two energy scans to average the absorption signal. In order to analyze the local symmetry, coordination number, valence, and local structure of samples a combined X-ray absorption near-edge structure (XANES) and

extended X-ray absorption fine structure (EXAFS) study is followed. The absorption spectra, normalized using standard procedures, are processed using Athena and Artemis software [36,37]. To obtain an estimate of the percentage of the α-Fe_3Si nanocrystals and the starting temperature where they are formed and embedded into the MWs, differential scanning calorimetric – thermogravimetric analyses (DSC-TGA) are carried out by a DSC/DTA/TGA Q600 module from TA Instruments with a rate of 5 ºC/min up to 1000 ºC in nitrogen atmosphere. Finally, the magnetic characterization of the selected MWs is performed using a physical property measurement system vibrating sample magnetometer (PPMS-VSM Model 6000 controller – Quantum Design) to obtain hysteresis loops under a maximum applied magnetic field of 1 T at room temperature.

2.3. High frequency characterization:

Radar absorbing paints are prepared mixing a total volume fraction ($V_{f,total}$) of 0.55% of MWs with a dielectric commercial paint. This $V_{f,total}$ contains different percentages of MWs with a length of 2 mm and 50 μm, obtained from ball milling, vacuum filtering and sedimentation processes (Figure 1). One slab of methacrylate with a thickness of 2.6 mm (Δ) is cut to fix our experimental dimensions (25 x 25 cm^2). This is used as support medium for the paint and serves to adjust the matching with the metal sheet to obtain a minimum of EM attenuation. The paint is sprayed on the methacrylate slab and the coating is dried for 24 h. The final thickness (t) of the composite (MWs and commercial paint) layer is 140 μm.

High frequency microwave attenuation characterization of the samples is performed using an experimental set-up that consists of a microwave anechoic chamber where two horn antennas (EMCO 3160-07) are placed in far-field conditions of the absorbing material [4,22]. Their bandwidth goes from 800 MHz to 19 GHz. The absorbing material is placed in front of one metallic plate to ensure total reflection conditions. The plates are surrounded by the same absorbers of the anechoic chamber to avoid border effects. Since the transmission EM horn antennas are in the far-field range, the EM waves can be considered as planar waves. The antennas are connected to a network analyzer (Agilent E8362B PNA Series Network Analyzer), and the scattering parameter S_{21} is measured, after careful calibration procedure based on open air measurements. Real and imaginary part of reflection coefficient (R_o) are obtained and the R_L defined as $R_L=20\log(|R_o|)$ (dB) is displayed. An illustration of the microwave absorption experimental set-up in reflection mode and a SEM image of one composite are shown in Figure 2.

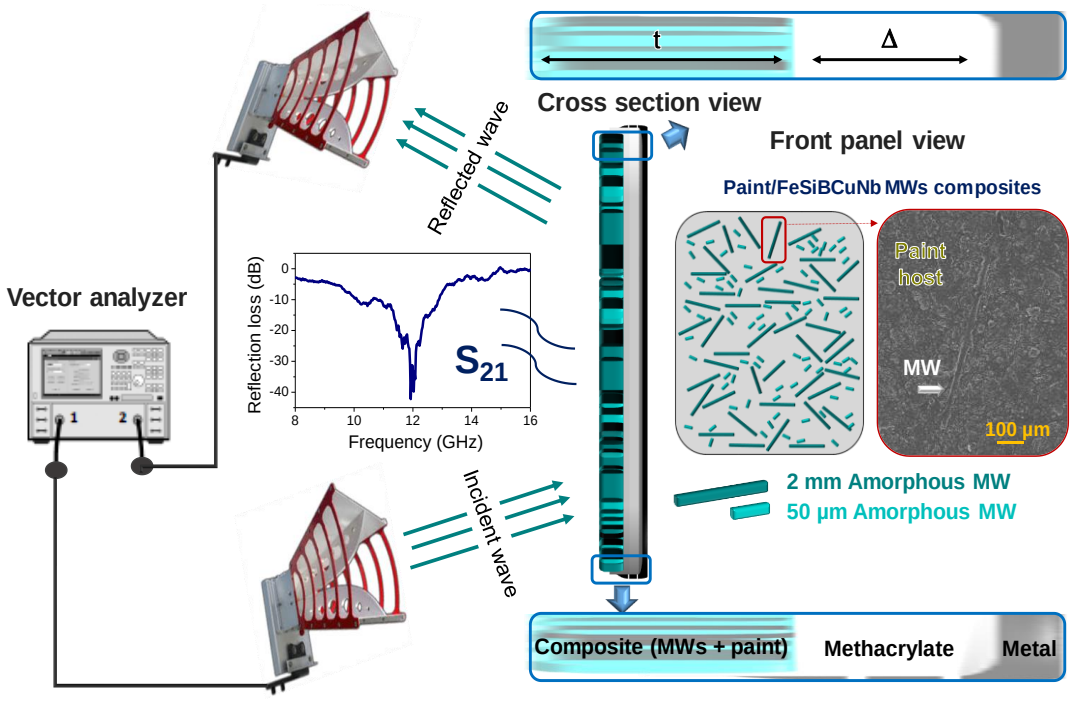

Figure 2. Schematic representation of the microwave absorption mechanism in reflection mode for composites based on commercial paint and selected $Fe_{73.5}Si_{13.5}B_9Cu_1Nb_3$ MWs (combined lengths of 2 mm and 50 µm). The thickness of the composite and the methacrylate slab is indicated as t and Δ respectively. A SEM image of the composite is added to show how the MWs are embedded in the commercial paint.

3. Results and discussion:

3.1. Morphological and structural characterization of the microstructures:

Figure 3 shows SEM images of the microstructure size evolution with milling time (2, 6 and 10 min) and the corresponding particle size distribution for as-cast and 550 ºC annealed MWs. The results reveal a gradual decrease of the MW length when milling time progresses, while the MW diameter is not significantly modified. Length size distributions follow a normal (Figure 3d) and log-normal (Figures 3e-f) functions with mean values ranging from 1300(1) µm to 144(2) µm for as-cast samples (Figures 3d-f) as the milling time increases. The annealed MWs exhibit a smaller order of magnitude with respect to the as-cast MWs probably due to the nanocrystallization process performed at 550 ºC, with mean values from 58(4) to 11.2(4) µm following a log-normal distribution (Figures 3j-l). During the annealing, the brittleness character increases considerably and enables smaller MW lengths and sharper distributions to be obtained than the as-cast ones. In contrast, ductile fracture of amorphous MWs means the loss of cylindrical geometry due to plastic deformation producing size distributions with larger lengths (Figures 3a-c).

The SEM results show that the cylindrical morphology is maintained for 2 and 6 min in both as-cast and annealed MWs, with size distributions much narrower for 6 min. Signs of flattening are identified for the microstructures prepared for 10 min of milling in the case of as-cast MWs (Figure 3c) and powder in the case of annealed ones. Therefore, the optimal milling time in maintaining homogeneous morphologies with relatively narrow size distributions is established as 6 min.

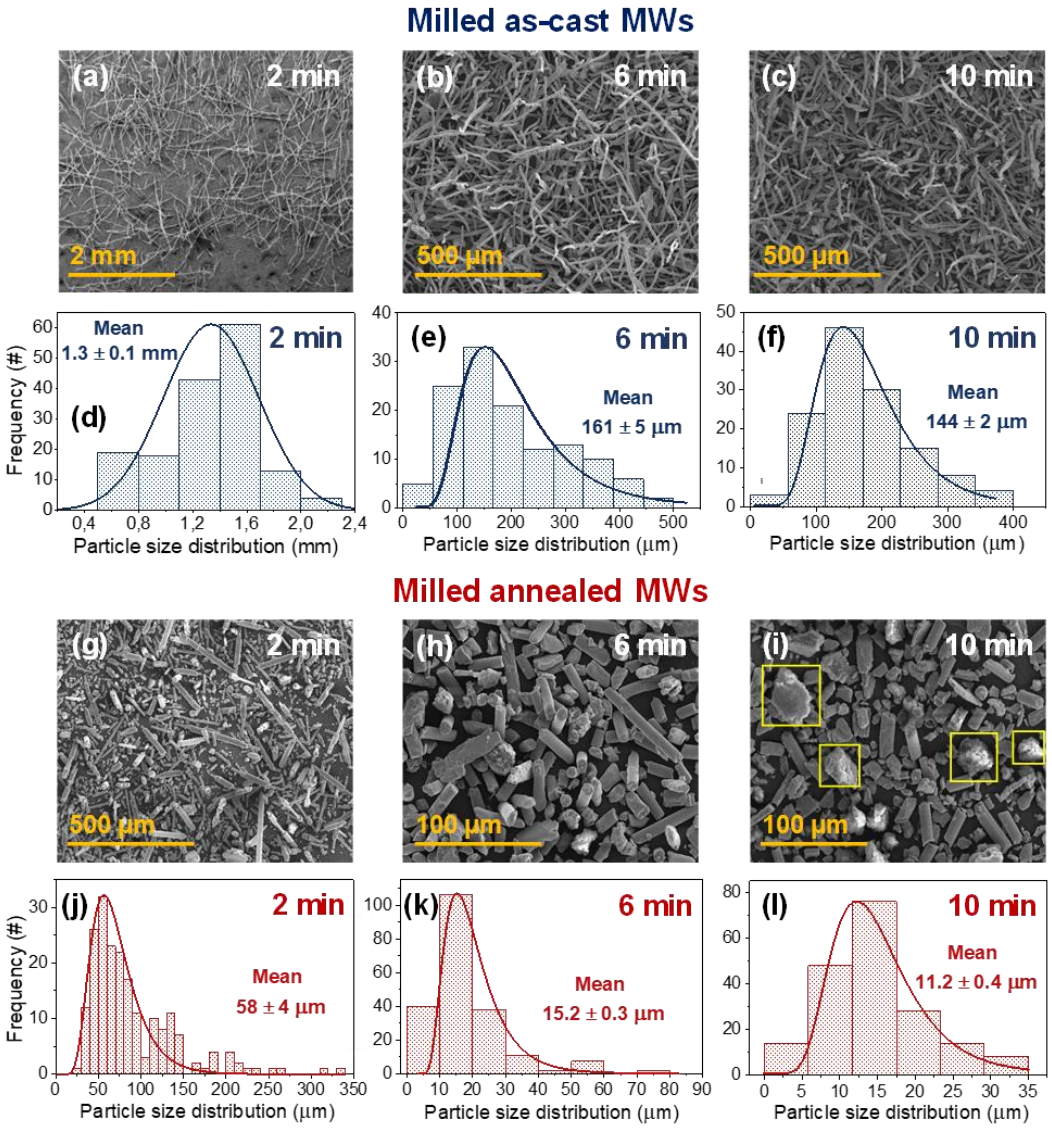

Figure 3. MWs length evolution for milling times of 2, 6 and 10 min: SEM images for (a-c) amorphous MWs and (g-i) 550 ºC annealed MWs and its length size distribution respectively, (d-f) for amorphous MWs and (j-l) for 550 ºC annealed MWs. Pyrex residues are found indicated with yellow square areas in Figure i.

The combination of vacuum filtering and sedimentation processes performed on the microstructures obtained after 6 min of milling process allows the material to be separated into refined products with selected narrower size distributions for amorphous MWs (Figures 4a-c)

and annealed (Figures 4d-f) MWs. Each batch has been divided according to three selected sizes obtained from settled-down (L), intermediate (M) and floating-up (S) regions during the sedimentation process (schematized in Figure 1). L, M and S mean distribution values for amorphous milled microstructures are respectively 419(9) µm, 246(8) µm and 50(3) µm. In contrast, for annealed microstructures, L, M and S mean distribution values are considerably reduced to 43.7(7) µm, 24.6 (8) µm and 11.7(2) µm respectively, where the fragile fracture is evidenced for nanocrystallized MWs. As a result, a cylindrical shape is more defined in annealed MWs than in ductile as-cast ones.

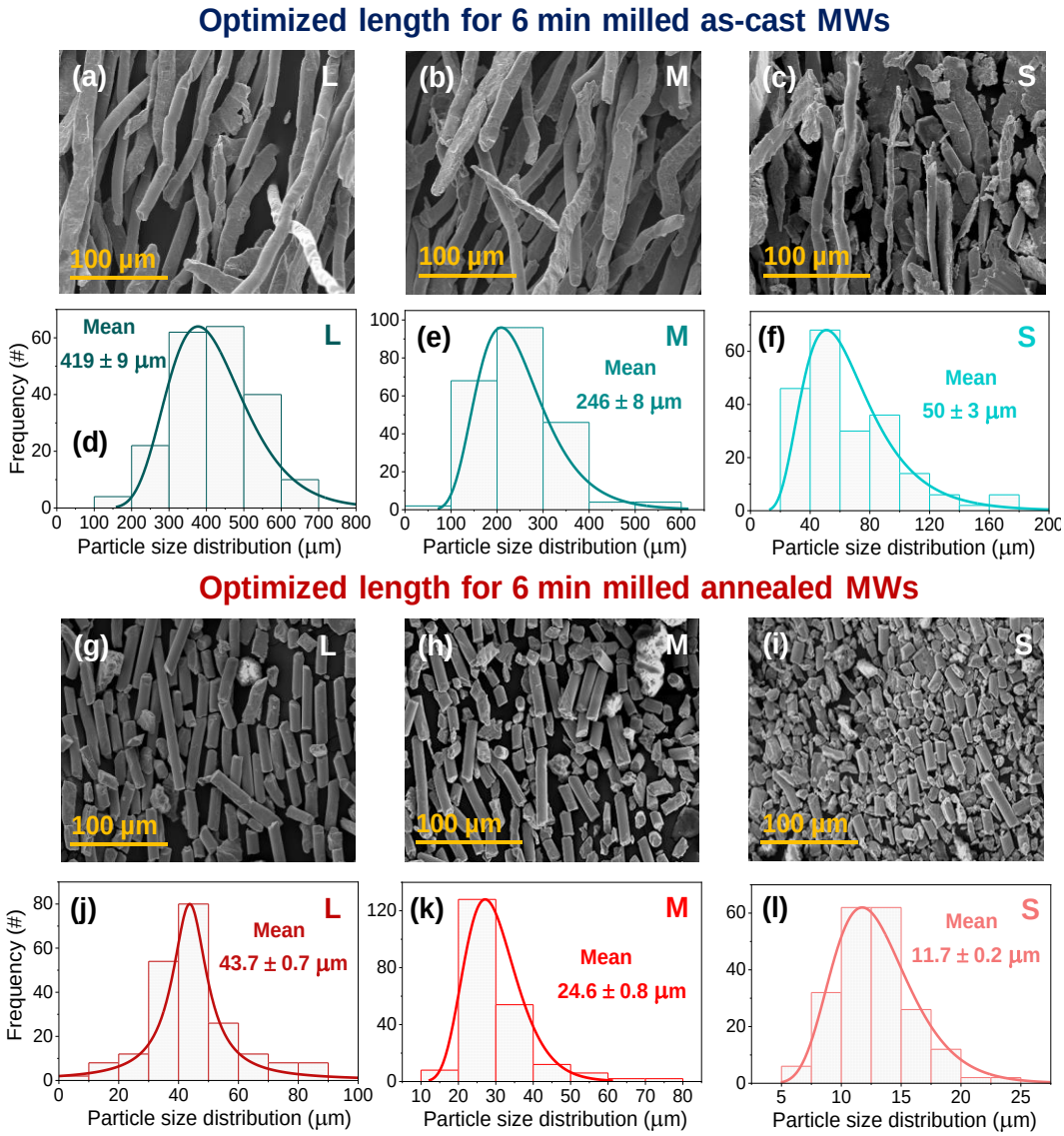

Figure 4. SEM images of 6 min ball-milled samples after vacuum filtering and sedimentation processes. Three different length ranges are selected for amorphous MWs: (a) L, (b) M and (c) S accompanied by their particle size distribution respectively (d-f). The same procedure is followed for annealed MWs: (g) L, (h) M and (i) S and their particle size distribution respectively (j-l).

XRD measurements are performed to find the crystalline evolution from as-cast and annealed samples to 6 min of milling (no length selection) (Figure 5). Below 30º, an amorphous shoulder is detected in each sample, normally due to amorphous silica coming from the pyrex coating [38]. The relative intensity of this shoulder increases when milling is performed (XRD patterns with light colors in Figure 5). This may be related to an increase in the number of defects associated with this process. Starting with the as-cast sample (dark blue XRD pattern), two other broad bumps are detected at around 44º and 80º related to amorphous Fe-based compounds [39]. When 6 min of milling is performed (light blue XRD pattern), the amorphous halo shape is slightly sharper. This effect could be attributed to an increase in the degree of crystallization with milling time [39,40]. By contrast, a partial nanocrystallization is exhibited in annealed samples with prominent diffraction peaks corresponding to α-Fe_3Si phase at 45.3º, 65.8º, 83.4º, 100.4º and 118.2º for (red XRD patterns) [41]. In these cases, no increase in the degree of crystallization are noted. To unveil the influence on the crystal domain size the Scherrer relation is employed [42]. For the amorphous sample the crystal domain size is 1.4(2) nm and for annealed sample is 12.5(1) nm. These values are similar to those found in the scientific literature [17,18,40,42,43] and therefore, a nanocrystallization process is achieved with the annealing performed at 550 ºC. Contrary for the annealed sample with 6 min of milling (light red XRD pattern), a decrease in crystalline domain size to 7.9(1) nm is obtained. This effect may be due to the generation of defects due to high energy impact processes during the milling [41].

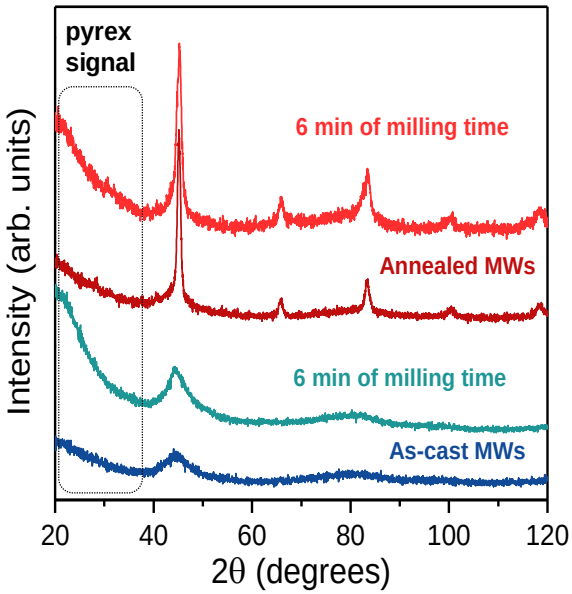

Figure 5. XRD patterns of as-cast MWs (dark blue), annealed MWs (dark red) and after 6 min of ball milling (light blue and light red respectively). Black rectangle indicates the amorphous contribution from pyrex XRD signature.

Regarding the degree of crystallization of the α-Fe_3Si compound induced by the annealing process, DSC-TGA measurements as a function of the temperature are carried out for as-cast and annealed samples (Figures 6a-b). T_1 and T_2 indicate the emergence of the α-Fe_3Si and Fe_2B nanocrystals (respectively), and their corresponding enthalpies ΔH_1 and ΔH_2 are calculated by integrating the area of the endothermic peaks detected (Figures 6a-b). The crystallization temperatures for as-cast sample are T_1 = 537 ºC and T_2 = 661 ºC and their enthalpies result in ΔH_1 = 71 and ΔH_2 = 38 J/g. In the case of the annealed sample, T_1 and T_2 present similar values and a decrease of ΔH_1 and ΔH_2 to 55 and 32 J/g respectively is obtained. The difference between enthalpies for ΔH_1 may imply ~23% percentage of nanocrystallized material for the sample treated at 550 °C [13]. In turn, nitriding evidence from 600 ºC is observed in both samples with a slight weight increase close to 1% at 1000 ºC (black curves in Figures 6a-b). This residual nitriding process is probably due to the presence of boron atoms in the pyrex coating of the MWs, which at temperatures above 600 ºC is energetically probable [45]. Nevertheless, this mechanism is barely noticeable at 550 °C (annealed temperature) and the physical properties of the MW are assumed to be unaffected by this process.

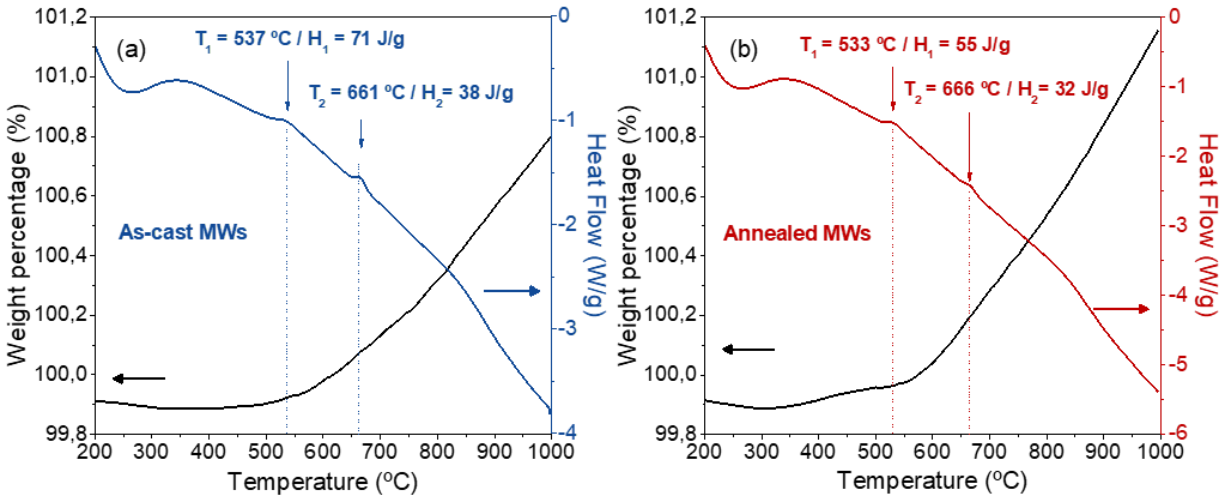

Figure 6. DSC-TGA curves performed from 200 ºC to 1000 ºC with a constant rate of 5 ºC/min for (a) as-cast and (b) annealed MWs. Crystallization temperatures (T_i) and enthalpy values (ΔH_i) are also represented in each case (i=1,2).

The oxidation state and structural modifications of MWs are analyzed by the XAS technique (Figure 7). XANES measurements performed at the Fe K-edge show a different absorption response for as-cast MWs compared with the Fe foil (reference) is observed, indicating a different coordination of Fe atoms and a low structural order in the FeSiBCuNb system. When MWs are annealed at 550 ºC (before milling), the XANES signal is modified which might involve a variation coming from the nanocrystallization process.

No changes in the energy position at the absorption edge of the XANES spectra are observed (first peak located at the same position in the first-derivative spectra in inset of Figure 7a). These results evidence the same valence state for as-cast MWs, after annealing performed at 550 ºC and Fe foil (oxidation state 0) [46–49].

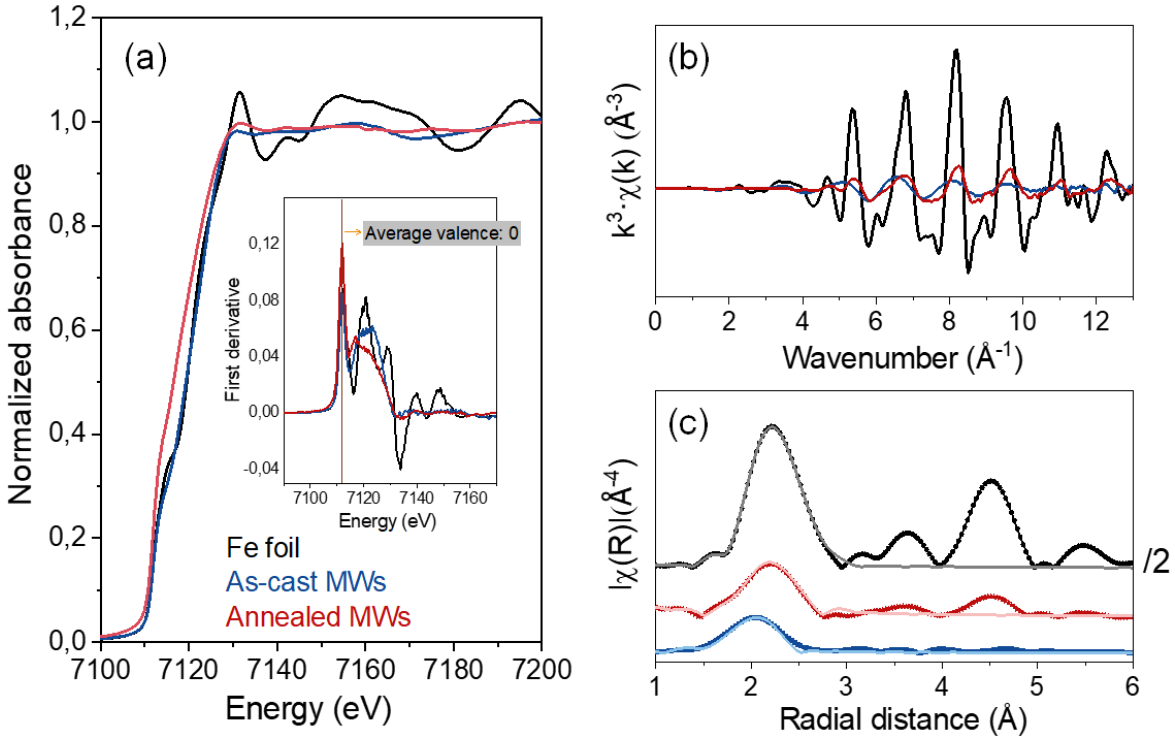

Figure 7. (a) XANES spectra, (b) k-space EXAFS curves and (c) FT modulus of the EXAFS signal (symbols) and best-fitting simulations (continuous lines) in the R range 1.5- 3 Å (first neighbors) for the as-cast and annealed MWs (2 mm length). Fe foil reference values are added for comparison.

The short range structure of Fe ions for as-cast amorphous MWs and after the annealing process is also evaluated by EXAFS measurements. The order of the first neighbors is analyzed in k-space for the different samples in the range from 2.1 to 12.5 $Å^{-1}$ with a k weight of 3. Figure 7b depicts the k-space EXAFS curves, detecting variations in both the intensity of oscillations and phase, and suggesting differences in the overall structure between the samples and with respect to the Fe foil. The Fourier transform (FT) of the oscillations provides the radial distribution function of the local structure which has been fitted within the real space range between 1 and 3 Å using the FEFFIT code (Figure 7c) [36,37]. Here, the shift at the edge energy previously calculated for the Fe foil is fixed. For the model, a single scattering is considered and two shells located at the first peak have been evaluated. The first one is composed by Fe-Fe interatomic distances and the second one consists of Fe-(Fe/Si) interatomic distances. The coordination number N, the interatomic distance R and the Debye-Waller (DW) factors σ^2 are used as free parameters for each fitting. The calculated EXAFS parameters are given in Table 1.

Table 1: N, R and DW factors of the first and second coordination shells obtained from experimental EXAFS results of the Fe foil, as-cast and annealed MWs.

Samples	First coordination shell (Fe-Fe)			Second coordination shell (Fe-Fe/Si)		
	N_1	R_1 (Å)	σ^2_1 (Å^2)	N_2	R_2 (Å)	σ^2_2 (Å^2)
Fe foil	8	2.471 (1)	0.0054 (1)	6	2.85 (1)	0.0076 (4)
Annealed MWs	2.09 (5)	2.467 (3)	0.0059 (3)	2.5 (3)	2.81 (3)	0.0190 (7)
Amorphous MWs	1.90 (4)	2.374 (4)	0.0098 (6)	-	-	-

In general terms, the Fe foil shows a well-defined EXAFS spectrum with a strong signal where the two coordination shells are fitted. By contrast, the amorphous MWs exhibits a considerably reduced signal, it being possible to fit only the first Fe-Fe shell. In addition, no short-range ordering at larger distances is noticeable probably due to the amorphous character of the Fe-based MWs as is also noticed in the XRD patterns (Figure 5). After annealing, the nanocrystallization of the MWs is well-defined through the EXAFS signal following the radial oscillations of Fe foil and suggesting a large crystalline character. In this case, a second shell is fitted which may be related to both Fe-Fe and Fe-Si interatomic distances. Therefore, the variations of the absorption signal in the XANES region suggest a different coordination compared with as-cast MWs and Fe foil reference (Table 1).

The nanocrystallization of the α-Fe_3Si is evidenced with an increase of the N related to the first shell (Fe-Fe interatomic distances) and the emergence of the new second shell arising after annealing (Fe-Fe/Si interatomic distances) (Figure 7c). This behavior is also noticeable at larger distances. In terms of the calculated fittings, the interatomic distance of the first coordination shell for amorphous MWs is located at ~2.37 Å and increases after annealing towards an interatomic distance similar to the Fe foil (~2.47 Å) (Table 1). The second shell of the annealed material also shifts towards lower distances with respect to the Fe foil, from ~2.85 to 2.81 Å, indicating structural deviations due to the Fe-Si bonds. Regarding the DW factors, a large structural disorder at short range for the amorphous MWs is obtained which decreases after annealing. However, the partial crystallization of the α-Fe_3Si compound is accompanied by an increase of the DW factor of the second shell. Therefore, the brittleness character of the annealed MWs may be influenced by this partial nanocrystallization.

3.2. Influence of the length optimization of the microstructures on the magnetic applications:

The magnetic properties of the microstructures obtained after 6 min of milling are compared to those of one single annealed MW (Figure 8a). The latter (black color) has a bistable behavior due to the longitudinal anisotropy induced by the pyrex [11]. A decrease of coercivity from 2 Oe for one single as-cast MW (not shown here) to 0.7 Oe is observed as a consequence of the emergence of α-Fe_3Si nanocrystals in single magnetic domain regime [17,18,43,50]. Taking into account this mechanism, the magnetic behavior of one single MW should be considered as the result of the counterbalance between the shape anisotropy and exchange coupling among nanocrystals given by the random anisotropy model [51]. In the case of nanocrystalline magnetic materials with randomly oriented easy axes in which the crystal domain size D is smaller than the ferromagnetic exchange length L_{ex}, the magnetization does not follow the local magnetic anisotropy axes and it is forced to align itself due to the exchange interaction. Thus, the effective anisotropy value is averaged over several grains, its magnitude is thereby reduced and therefore its coercivity [17].

Comparing with the hysteresis loop related to one single annealed MW (black color), a noticeable increase in coercivity and a decrease in remanence is observed after 6 min of milling for both as-cast and annealed MWS (Figure 8a). On one hand, an increased coercivity might be mainly associated with the formation of microstructural defects during the milling process that act as pinning for the magnetic domain walls [52]. On the other hand, remanence is intimately related to the shape anisotropy and therefore, it is lower as the length of the MW decreases (Figure 8a) [15].

This variation in coercivity is much more pronounced when the optimization of the length regions (L, M and S) is carried out by combined vacuum filtering and sedimentation processes, confirming the trends observed in Figure 8a. With this length selection, the hysteresis loops show a progressive decrease in remanence and coercivity when the mean length of the microstructures is diminished for as-cast MWs (blue lines in Figure 8b), and continues for annealed MWs (red lines in Figure 8b). Specifically, the optimization length from as-cast material shows a slight decrease from 31 to 17 Oe with a length variation from 419 to 50 μm. In contrast, these variations are more noticeable in the optimized microstructures coming from the annealed samples with a drop from 20 to 0.1 Oe for length distributions ranging from 44 to 12 μm (Figure 8c).

The reduced coercive field values of the microstructures with smaller lengths can be justified considering the dipolar field acting on each individual MW due to all surrounding ones (Figures 8b-c). This dipolar field is higher when the length of the MWs decreases due to the increase of the axial demagnetizing factor.

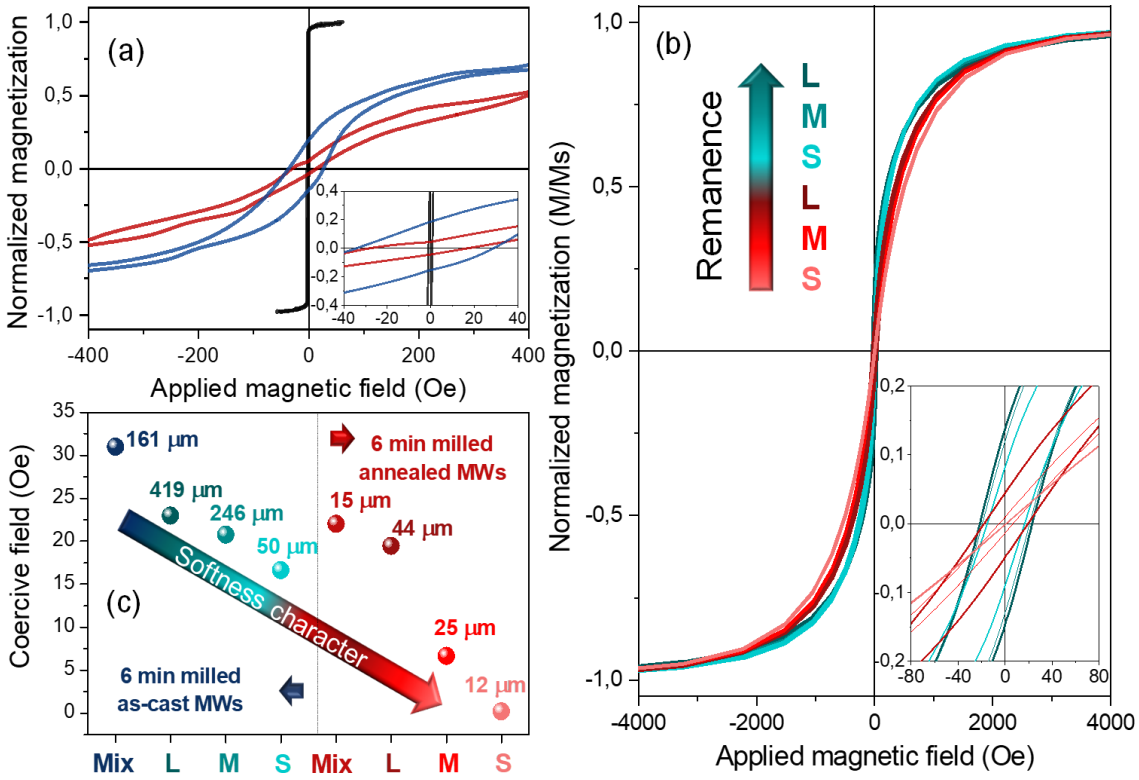

Figure 8. Room temperature magnetic behavior: Hysteresis loops for (a) one single annealed MW (black line) and microstructures obtained after 6 min of ball milling time performed in as-cast (blue line) and annealed (red line) MWs, and for (b) L, M and S length regions obtained by vacuum filtering and sedimentation processes from 6 min of ball milling time in each case. (c) Representation of the L, M and S optimized length regions as a function of the coercivity corresponding to as-cast and annealed MWs. Mean length values are those calculated by SEM analyses (Figure 4). Results of mixed MW lengths are also added for comparison in both cases. Insets on (a) and (c) show a magnification of the central area for clarity.

Finally, the balance between the shape and magnetoelastic anisotropies is taken into account in order to explain the variation in coercivity between different sizes of as-cast and annealed samples (separately). Concerning the shape anisotropy, an increase of the axial demagnetizing factor is favored with a decrease of the length of the MW. This effect leads to a lower longitudinal anisotropy term with no critical switching field, which makes easier the total magnetization process easier. Applying this approach to the behavior shown in Figure 8b, this effect is evident as the size of the microstructures decreases.

Regarding the variations in coercivity, the ball milling technique is known as an effective method to introduce a high dislocation density and other structural defects [39]. According to the Neel's theory [53], the random distribution of the internal stresses σ introduced by milling in a sample with local magnetostriction constant λ are expected to increase the coercivity. If the magnetoelastic energy term λσ is larger than the shape anisotropy, the coercivity is predicted to be proportional to $\nu^*(\lambda Y\varepsilon)/M_s$, where ν^* is the strained volume fraction, ε is the strain lattice, Y the elastic constant and M_S is the saturation magnetization [51]. According to this, the ductile character would promote a higher number of structural defects with larger MW length and present an increased coercivity (Figures 8b-c). Due to the nanocrystallized microstructure of the annealed samples with their subsequent brittle character, the magnetoelastic energy is considerably reduced in this instance. For this reason, it is proposed that the brittle character of the annealed MWs plays an important role during the ball milling process. The annealed MWs break down into smaller microstructures before creating huge structural defects that would anchor the magnetic domain walls. This effect could be reflected in a well-defined cylindrical shape in the annealed case as evidenced by the SEM images (Figures 3-4) and would lead to a progressive decrease in coercivity as shown in Figure 8c. Here, the length particle distribution influence on coercivity is sumarized for amorphous and annealed MWs respectively confirming this general trend. With these results, the optimization carried out on the length distributions of the microstructures is achieved by tuning the magnetic properties with high technological potential and the values of coercivity and remanence are discretized compared to mixed samples.

3.3. Influence of the length optimization of the microstructures on the microwave absorption applications:

Further to the understanding of the magnetic behavior of the optimized length MWs and their tunability of the remanence and coercivity, this section targets the microwave tunable properties of composites based on commercial paint for the radar application range. The aim is to obtain tunability of the absorption frequency with neglected magnetic and conductive losses by varying the partial volumen fraction ($V_{f,i}$) in the mixture coming from different optimized length MW distributions (i), but keeping constant the $V_{f,total}$. For this purpose, composite sheets are manufactured with randomly distributed MWs and whose $V_{f,total}$ is below the percolation threshold p_c [8]. Then, a metallic sheet is covered by a double layer formed by a first dielectric slab (Δ = 2.6 mm) and the thickness of the composite (t = 140 μm). The characteristics of the experiment for microwave attenuation are described below and shown in Figure 2.

There are numerous theories and numerical models applied to different systems to determine the p_c [34,54,55]. The composites fabricated in this work are based on a continuous medium enveloping the conducting inclusions and its most experimentally and theoretically consistent expression is $p_c \sim D_{total} / L$, where L is the MW length [55]. Specifically, the five composites prepared have $V_{f,total} = 0.55\%$ but different p_c depending on the substitution degree of the MW length distribution to fine-tune the frequency of the microwave absorption. This approach consists of substituting different $V_{f,2mm}$ of as-cast 2 mm length MW with $V_{f,50\ \mu m}$ of 50 µm length MW (Figures 4c and 4f), as an example of potential applicability (Figure 2). For performance in the radar operating range, the diameter employed for 2 mm length MWs is 19.8 µm (composed by pyrex coating with a thickness of 15.8 µm and a metallic nucleus diameter of 4 µm) and their $V_{f,2mm}$ chosen goes from 0.55% (Composite 1) to 0.19% (Composite 5) (Table 2). The minimum value of the p_c is 0.99% and is obtained for the Composite 1. For the rest of the composites, substituting percentages of MWs with MWs of 50 µm length will increase the p_c value and the $V_{f,total}$ will be further below it.

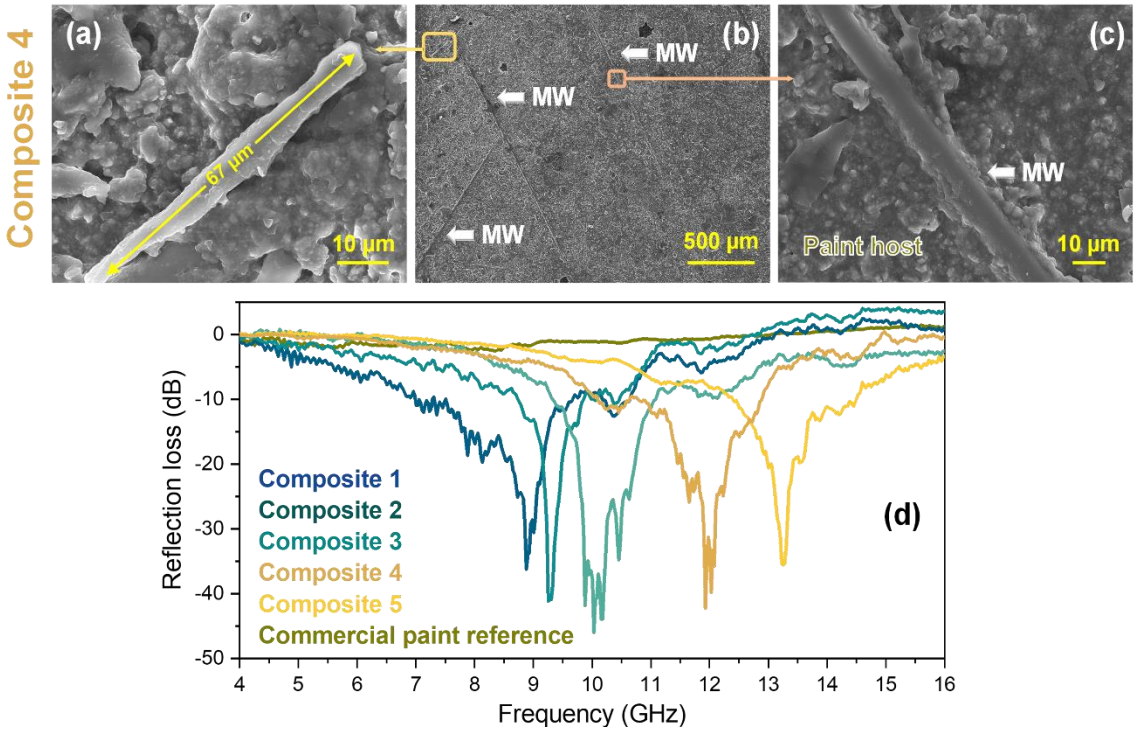

Figure 9. (a-c) SEM images of the Composite 4 with $V_{f,2mm} = 0.30$ and $V_{f,50\mu m} = 0.25$. Image A shows a detail of one MW obtained from as-cast S region (marked with a yellow rectangle in the upper left region in image B). Image C displays a detail of one section of 2 mm length MW embedded in the paint host (indicated with a orange rectangle angle in the top center region in image B. (d) Tunability of MWs as absorber microwave materials: R_L curves as a function of the frequency (4-16 GHz) obtained from composites prepared with different $V_{f,2mm}$ and $V_{f,50\mu m}$ mixed with commercial paint (added as a reference in dark yellow color). Detail information about the percentages can be found in Table 2.

Figure 9 shows the frequency dependence of the average R_L obtained for the composites under study (Table 2). In all samples, the R_L curves exhibite strong absorptions in the radar window with a lowest resonance frecuency located at 8.75 GHz (Composite 1). As the $V_{f,2mm}$ is replaced by $V_{f,50\mu m}$, this minimum progresively blueshifts up to 13.25 GHz (Composite 5). Relatively high intensity absorptions ranging from -35.42 dB (Composite 5) up to -45.97 dB (Composite 3) are observed, and no significant changes in the bandwiths are obtained. The experimental absorption frequencies with their corresponding minimum R_L values are displayed in Table 2.

Generally speaking, the electromagnetic absorption mechanisms of these kind of composites based on metallic inclusions (MWs) depend strongly on the p_c [8,34,54,55]. This crucial value determines the different contributions that can dominate the microwave absorption. Above p_c, the microwave absorption originates from magnetic losses (for example magnetostatic energy and/or NFMR) and below p_c, from dielectric losses (polarization and/or conduction loss regimes) [8,56]. Related to magnetic losses, $V_{f,total}$ (below the p_c) results in the spacing of the MWs causing a negligible magnetostatic interaction and a reduced NFMR effect coming from the precession of the magnetic moment [4,8,31,56].

Excluding a magnetic origin, a dominant absorption mechanism by dielectric losses is proposed for these composites [8,56]. In this context, conductive losses are also ruled out as $V_{f,total}$ is below the p_c and there is no direct contact between the metal inclusions [8]. Therefore, the origin of the absorption is mainly due to polarization dielectric losses. When the electromagnetic wave interacts with the composite, the MWs behave as a dipolar antennas and the interference pattern formed causes an absorption minimum [22]. Considering a homogeneous 3D spatial distribution of all inclusions in the composites and that the electromagnetic wavelengths are larger compared to the sizes of the inclusions (quasistatic conditions), an effective medium standard model for electrical permittivity ε_{eff} can be applied based on the Maxwell-Garnett model [32–34].

Equation (1)

$$\varepsilon_{eff} = \varepsilon_{host} + \frac{\frac{1}{3}\sum_{i=1}^{n} V_{f,i}\,(\varepsilon_{inclusion}-\varepsilon_{host})\sum_{k=1}^{3}\frac{\varepsilon_{host}}{\varepsilon_{host}+N_{i,k}(\varepsilon_{inclusion}-\varepsilon_{host})}}{1-\frac{1}{3}\sum_{i=1}^{n} V_{f,i}\,(\varepsilon_{inclusion}-\varepsilon_{host})\sum_{k=1}^{3}\frac{N_{i,k}}{\varepsilon_{host}+N_{i,k}(\varepsilon_{inclusion}-\varepsilon_{host})}}$$

where ε_{host} is the relative permittivity; $\varepsilon_{inclusion}$ is the relative permittivity of the MWs; $V_{f,i}$ is the volume fraction occupied by the i-MWs; $N_{i,k}$ are the depolarization factors of the i-MWs, and the index k = 1, 2, 3 corresponds to x, y, and z cartesian coordinates. Below p_c range, the permittivity and permeability curves are almost constant in the studied microwave window [57] as shown in other works with magnetic inclusions with the same MW composition ($Fe_{73.5}Si_{13.5}Nb_3Cu_1B_9$), with a length of 1-2 mm and a $V_{f,total}$ of 1% [8]. Moreover, for inclusions with a conductivity σ

= 0.8×10^6 S/m in the frequency range ~10^{10} Hz, has a $\varepsilon_{inclusion}$ value seven or eight order of magnitude larger than the ε_{host} ($\varepsilon_{inclusion} = j\ \sigma/\omega$). Therefore, the generalized Maxwell-Garnet expression considering ellipsoidal inclusions can be simplified for the following approximation [55]:

Equation (2) $$\varepsilon_{eff} \approx \varepsilon_{host}\left(1 + \frac{V_{f,i}}{3N_z}\right)$$

In our case, i referes to 2 mm and 50 μm length and ε_{host} referes to the paint electrical permitivity ($\varepsilon_{host} = 3$ [8,22]). This is valid for $N_z\ \varepsilon_{inclusion} >> \varepsilon_{host}$ where N_z is the depolarizing factor along the MWs length that can be approached by:

Equation (3) $$N_{z\,(D_{core},L)} = \left({}^{D_{core}}/_{L}\right)^2 \ln\left(\frac{L}{D_{core}}\right)$$

where D_{core} and L are the diameter and the length of the metal MWs that are always in the range of few microns. By applying this expression to the two MW sizes, $N_{z\,(D_{core},L)}$ we obtain $N_{z\,(4\ \mu m,2\ mm)} = 2.48\ 10^{-5}$ and $N_{z\,(9.4\ \mu m,50\ \mu m)} = 5.91\ 10^{-2}$. Subsequently, the ε_{eff} is calculated for the five composites and are presented in Table 2.

On the other hand, assuming this system as a double layer a minimum return loss, R_{Lmin} is observed for certain matching conditions that depend on Δ, t and ε_{eff}. The attenuation produced by the double layer can be exactly predicted by considering the interference pattern formed and the effective medium standard model for electrical permittivity. This phenomenon can be explained by the 1/4 wavelength cancellation equation [58,59], which is given for a single layer absorber by:

Equation (4) $$f_{min} = \frac{c}{4t\sqrt{\varepsilon_{eff}}}$$

where c is the light speed, and t is the layer thickness of the composite. In the case of double layer a good aproximation for the f_{min} is given by:

Equation (5) $$f_{min} = \frac{c}{4\sqrt{\varepsilon_{eff}}\sqrt{t\,\Delta}}$$

In this scenario, the f_{min} is calculated for the fixed thicknesses Δ and t and considering the ε_{eff} previously calculated. These calculated values are compared with the experimental ones in Table 2. The change of the MW amount has an impact on the double layer in terms of the attenuation band. The frequency of the $R_{L,min}$ blueshifts with higher substitution percentage of 50 μm length MWs. There are slight deviations from the value calculated being maximum in the Composite 1

and 4. The reason of these deviations is likely due to the fact that the values of 2 mm and 50 µm are mean values and they have their corresponding length distributions. Even so, these results are consistent with the experimental measurements and the prediction of the $R_{L,min}$ position in the radar attenuation range is provided through this work.

Table 2: Composite microwave absorption properties with different $V_{f,2mm}$ and $V_{f,50\mu m}$ (ε_{host} = 3 [8,22]). Calculated (Equation 4) and experimental frequency on minimum $R_{L,min}$ are also included.

Samples	$V_{f,2\ mm}$	$V_{f,50\ \mu m}$	$\varepsilon_{eff} \approx \varepsilon_{host}\left(1+\frac{V_{f,i}}{3N_{z,i}}\right)$	$f_{min,calculated} = \frac{c}{4\sqrt{\varepsilon_{eff}}\sqrt{t\Delta}}$	$f_{min,experimental}$	$R_{L,min}$
1	0.55%	0.00%	ε_{host} (74.75)	8.30 GHz	8.85 GHz	-36.21 dB
2	0.45%	0.10%	ε_{host} (62.35)	9.09 GHz	9.28 GHz	-40.96 dB
3	0.36%	0.19%	ε_{host} (50.28)	10.12 GHz	10.03 GHz	-45.97 dB
4	0.30%	0.25%	ε_{host} (42.24)	11.04 GHz	11.98 GHz	-42.23 dB
5	0.19%	0.36%	ε_{host} (27.49)	13.68 GHz	13.25 GHz	-35.42 dB

To finish the discussion on this work a revision of the microwave absorbing state of the art is carried out drawing an analogy with other fillers employed. All investigations are also based on different physical strategies to obtain an optimization of the absorption in the range (1-18 GHz). The constituents of the manufactured composites are shown in Table 3 and the $V_{f,total}$, $R_{L,min}$ and their associated absoption frequencies are added for comparison. High $R_{L,min}$ values can be seen in most of the studies, with Fe_3O_4@N-doped carbon nanochains [60] and Fe_3Si-core/amorphous-C-shell nanocapsules [61] with high responses of -63.09 dB (11.91 GHz) and -68.3 dB (13 GHz) respectively. Compared to the results obtained in this work based on $Fe_{73.5}Si_{13.5}Nb_3Cu_1B_9$ MWs/commercial paints, $R_{L,min}$ also has a large value of -45.97 dB (10.03 GHz) but 27% and 32.69% lower respectively. However, 18% and 99.45% increase in the $V_{f,total}$ are used respectively in those investigations. Therefore, depending on the parameters to be compared, one or another efficient absorption strategy prevails in the range (1-18 GHz). Similarly, these results provided show that are highly competitive and open a large field of research by proposing selected length distributions of MWs as powerful microwave absorbers with relatively low filling percentages (0.55%, below p_c), with negligible magnetic and conductive losses. Furthermore, tuneability in frequencies is demonstrated with this example and the range of frequencies of applicability can be extended by varying the thickness of the layer Δ (higher thickness - range displaced to lower frequencies) and/or by adding other length MW distributions (shorter lengths - range displaced to higher absorption frequencies).

Table 3: Microwave absorption performance of reported composites.

Absorbing composites – Host matrix	Weight or Volumen fraction	R_{Lmin} values	Frequency values	Reference
MWCNTs – epoxy resin	4%	-19 dB	6 GHz	[62]
Copper MWs – Commercial paint	0.55%	-27 dB	10.7 GHz	[22]
Ni fibers – PES	7%	-58 dB	1-2 GHz	[63]
Ni powder – SIM-2030M	8.7%	-50 dB	1-2 GHz	[64]
$Co_{68.7}Fe_4Ni_1B_{13}Si_{11}Mo$ wires – 913 E-glass prepegs	0.026%	-18 dB	1-2 GHz	[65]
Fe_3O_4@N-doped carbon nanochains – Paraffin	20%	-63.09 dB	11.91 GHz	[60]
Fe_3O_4@C nanosheets – Paraffin	40%	-46 dB	12.8 GHz	[66]
Fe_3O_4@C nanofibers – Paraffin	5%	-46 dB	7.8 GHz	[67]
Fe_3Si-core/amorphous C-shell nanocapsules – Paraffin	50%	-68.3 dB	13 GHz	[61]
Elliptical Fe_3O_4 nanorings – Paraffin	11%	-58.88 dB	17.68 GHz	[59]
Fe_3O_4/Graphene capsules – Paraffin	30%	-32 dB	8.76 GHz	[26]
Laminated MXene/Ni – MXene	0.01%	-50.5 dB	5.5 GHz	[27]
Peapod-like MnO/C nanowires – Paraffin	10%	-55 dB	13.6 GHz	[28]
NiO nanorings/SiC – NiO/SiC	1-3%	-50 dB	10.5 GHz	[29]
GeP nanosheets – Paraffin wax	30%	-37.8 dB	4.7 GHz	[30]
Fe_3Si/SiC fibers – Silicon resin	1.6%	-22 dB	16 GHz	[68]
Fe_3Si/SiC fibers – Silicon resin	5%	-30.1 dB	11.9 GHz	[68]
Fe_3Si/SiC – Silicon oxide	30%	-37.53 dB	15.5 GHz	[69]
$Fe_{89}Si_3B_1C_3Mn_4$ MWs – Commercial paint	2%	-35 dB	8.5 GHz	[4]
$Fe_{73.5}Si_{13.5}Nb_3Cu_1B_9$ MWs – Commercial paint	0.55%	-45.97 dB	10.03 GHz	Herein

4. Conclusions

Fine-tune control in the length of as-cast and 550 ºC annealed $Fe_{73.5}Si_{13.5}Nb_3Cu_1B_9$ MWs is performed by combination of high-energy ball milling, vacuum filtration and subsequent sedimentation processes. Relatively sharp mean size distribution values ranging from 1300 μm to 11.2 μm are achieved and the smallest lengths are obtained when a thermal treatment is carried out at 550 ºC in nitrogen atmosphere. During this annealing, a generalized fragilization of the material is promoted by the formation of α-Fe_3Si nanocrystals. The MW lengths and their structural features have an influence on the magnetic behavior for amorphous and nanocrystallized microstructures, showing a general tendency: the shorter is the microstructure length the lower is the coercivity and remanence magnetization, being this effect more striking for the nanocrystallized material.

Promising experiments are performed in composites composed by the optimized microstructures (2 mm and 50 μm length MWs) and commercial paints for an effective

microwave attenuation. These composites exhibit a blueshift of the attenuation frequency from 8.85 GHz (Composite 1) up to 13.25 GHz (Composite 5) with high values of $R_{L,min}$ between -35.42 dB (Composite 5) and -45.97 dB (Composite 3). These experimental results are confirmed by an effective medium standard model (Maxwell-Garnett approximation) proposed for electrical permittivity testing its outstanding consistency. Therefore, the tunability and multifunctionality of as-cast and annealed $Fe_{73.5}Si_{13.5}Nb_3Cu_1B_9$ MWs by optimizing their length is identified in magnetic and microwave absorbing applications.

Author Contributions

The manuscript was written through contributions of all authors. All authors have given approval to the final version of the manuscript.

Funding Sources

Financial support from the Spanish Ministry of Science, Innovation and Universities under the projects RTI2018-095856-B-C21, MAT2017-86540-C4-1-R and RTI2018-095303-A-C52, from Comunidad de Madrid NANOFRONTMAG S2013/MIT-2850 and NANOMAGCOST S2018/NMT-4321. A.S. acknowledges the financial support from the Comunidad de Madrid for an "Atracción de Talento Investigador" contract (No. 2017-t2/IND5395).

Acknowledgments

The European Synchrotron (ESRF), MCIU and Consejo Superior de Investigaciones Cientificas (CSIC) are acknowledged for the provision of synchrotron radiation facilities. We also thank Dr. Charles Eduard Creffield for his supervision and the BM25-SpLine staff for the technical support beyond their duties.

References

[1] Qin, F.; Peng, H. X.; Tang, J.; Qin, L. C. Ferromagnetic Microwires Enabled Polymer Composites for Sensing Applications, *Compos. Part A Appl. Sci. Manuf.* **2010**, 41, 1823-1828.

[2] Marín, P.; Marcos, M.; Hernando, A. High Magnetomechanical Coupling on Magnetic Microwire for Sensors with Biological Applications, *Appl. Phys. Lett.* **2010**, 96, 262512.

[3] Kurlyandskaya, G. V.; Giant Magnetoimpedance for Biosensing: Advantages and Shortcomings, *J. Magn. Magn. Mater.* **2009**, 321, 659-662.

[4] Marín, P.; Cortina, D.; Hernando, A. Electromagnetic Wave Absorbing Material Based on Magnetic Microwires, *IEEE Trans. Magn.* **2008**, 44, 3934-3937.

[5] Richter, K.; Varga, R.; Badini-Confalonieri, G. A.; Vázquez, M. The Effect of Transverse Field on Fast Domain Wall Dynamics in Magnetic Microwires, *Appl. Phys. Lett.* **2010**, 96, 182507.

[6] Morales, I.; Archilla, D.; de la Presa, P.; Hernando, A.; Marín, P. Colossal Heating Efficiency Via Eddy Currents in Amorphous Microwires with Nearly Zero Magnetostriction, *Sci. Rep.* **2020**, 10, 1–14.

[7] Zhukov, A.; Rodionova, V.; Ilyn, M.; Aliev, A. M.; Varga, R.; Michalik, S.; Aronin, A.; Abrosimova, G.; Kiselev, A.; Ipatov, M.; Zhukova, V. Magnetic Properties and Magnetocaloric Effect in Heusler-Type Glass-Coated NiMnGa Microwires, *J. Alloys Compd.* **2013**, 575, 73-79.

[8] Qin, F.; Peng, H.-X. Ferromagnetic Microwires Enabled Multifunctional Composite Materials, *Prog. Mater. Sci.* **2013**, 58, 183–259.

[9] Larin, V. S.; Torcunov, Zhukov, A. V.; González, J.; Vázquez, M.; Panina, L. Preparation and Properties of Glass-Coated Microwires, *J. Magn. Magn. Mater.* **2002**, 249, 39–45.

[10] Vázquez, M.; Zhukov, A. P. Magnetic Properties of Glass-Coated Amorphous and Nanocrystalline Microwires, **1996**, 160, 223–228.

[11] Zhukov, A.; Vázquez, M.; Velázquez, J.; Hernando, A.; Larin, V. S. Magnetic Properties of Fe-Based Glass-Coated Microwires, *J. Magn. Magn. Mater.* **1997**, 170, 323-330.

[12] González, J.; Murillo, N.; Larin, V. S.; Barandiaran, J. M.; Vázquez, M.; Hernando, A. Magnetic Bistability of Glass-Covered Fe-Rich Amorphous Microwire: Influence of Heating Treatments and Applied Tensile Stress, *Sensor Actuat. A-Phys.* **1997**, 59, 97-100.

[13] Marín, P.; Vázquez, M.; Olofinjana, A. O.; Davies, H. A. Influence of Cu and Nb on Relaxation and Crystallization of Amorphous FeSiB(CuNb) Wires, *Nanostruc. Mater.* **1998**, 10, 299–310.

[14] Vázquez, M.; Knobel, M.; Sánchez, M. L.; Valenzuela, R.; Zhukov, A. P. Giant Magnetoimpedance Effect in Soft Magnetic Wires for Sensor Applications, *Sensor Actuat. A-Phys.* **1997**, 59, 20-29.

[15] Herrero-Gómez, C.; Marín, P. Hernando, A. Bias Free Magnetomechanical Coupling on Magnetic Microwires for Sensing Applications, *Appl. Phys. Lett*. **2013**, 103, 142414.

[16] Zhukov, A.; Cobeño, A. F.; González, J.; Torcunov, A.; Pina, E.; Prieto, M. J.; Blanco, J. M.; Larin, V. S.; Baranov, S. Ferromagnetic Resonance, Magnetic Behaviour and Structure of Fe-Based Glass-Coated Microwires, *J. Magn. Magn. Mater.* **1999**, 203, 238–240.

[17] Herzer, G. Grain Size Dependence of Coercivity and Permeability in Nanocrystalline Ferromagnets, *IEEE Trans. Magn.* **1990**, 26, 1397–1402.

[18] Herzer, G. Grain Structure and Magnetism of Nanocrystalline Ferromagnets, *IEEE Trans. Magn.* **1989**, 25, 3327–3329.

[19] Skorvánek, I.; Svec, P.; Grenèche, J. M.; Kovác, J.; Marcin, J.; Gerling, R. Influence of Microstructure on the Magnetic and Mechanical Behaviour of Amorphous and Nanocrystalline FeNbB Alloy, *J. Phys. Condens. Matter.* **2002**, 14, 4717-4736.

[20] Marín, P.; Cortina, D.; Gorriti, A.; Hernando, A. Electromagnetic-Radiation Attenuator and Method for Controlling the Spectrum Thereof, **2011**, International Patent Number: WO 2010/029193.

[21] Gorriti, A.; Cortina, D.; de la S. Flores, M.; Robledo, J. S.; Robledo, J. J. G.; Marín, P.; Hernando, A. Electromagnetic Radiation Attenuator, **2015**, International Patent Number: WO 2013/144410.

[22] Gorriti, A. G.; Marín, P.; Cortina, D.; Hernando, A. Microwave Attenuation with Composite of Copper Microwires, *J. Magn. Magn. Mater.* **2010**, 322, 1505-1510.

[23] Zhang, Y.; Huang, Y.; Zhang, T.; Chang, H.; Xiao, P.; Chen, H.; Huang, Z.; Chen, Y. Broadband and Tunable High-Performance Microwave Absorption of an Ultralight and Highly Compressible Graphene Foam, *Adv. Mater.* **2015**, 27, 2049–2053.

[24] Li, X.; Feng, J.; Du, Y.; Bai, J.; Fan, H.; Zhang, H.; Peng, Y.; Li, F. One-Pot Synthesis of $CoFe_2O_4$ /Graphene Oxide Hybrids and their Conversion into FeCo/Graphene Hybrids for Lightweight and Highly Efficient Microwave Absorber, *J. Mater. Chem. A.* **2015**, 3 5535–5546.

[25] Han, M.; Yin, X.; Hou, Z.; Song, C.; Li, X.; Zhang, L.; Cheng, L. Flexible and Thermostable Graphene/SiC Nanowire Foam Composites with Tunable Electromagnetic Wave Absorption Properties, *ACS Appl. Mater. Interfaces.* **2017**, 9, 11803–11810.

[26] Jian, X.; Wu, B.; Wei, Y.; Dou, S. X.; Wang, X.; He, W.; Mahmood, N. Facile Synthesis of Fe_3O_4/GCs Composites and their Enhanced Microwave Absorption Properties, *ACS Appl. Mater. Interfaces.* **2016**, 8, 6101–6109.

[27] Li, X.; You, W.; Wang, L.; Liu, J.; Wu, Z.; Pei, K.; Li, Y.; Che, R. Self-Assembly-Magnetized MXene Avoid Dual-Agglomeration with Enhanced Interfaces for Strong Microwave Absorption through a Tunable Electromagnetic Property, *ACS Appl. Mater. Interfaces.* **2019**, 11, 44536–44544.

[28] Duan, Y.; Xiao, Z.; Yan, X.; Gao, Z.; Tang, Y.; Hou, L.; Li, Q.; Ning, G.; Li, Y. Enhanced Electromagnetic Microwave Absorption Property of Peapod-like MnO@carbon Nanowires, *ACS Appl. Mater. Interfaces.* **2018**, 10, 40078–40087.

[29] Yang, H.-J.; Cao, W.-Q.; Zhang, D.-Q.; Su, T.-J.; Shi, H.-L.; Wang, W.-Z.; Yuan, J.; Cao, M.-S. NiO Hierarchical Nanorings on SiC: Enhancing Relaxation to Tune Microwave Absorption at Elevated Temperature, *ACS Appl. Mater. Interfaces.* **2015**, 7, 7073–7077.

[30] Chang, Y.; Mu, C.; Yang, B.; Nie, A.; Wang, B.; Xiang, J.; Yang, Y.; Wen, F.; Liu, Z. Microwave Absorbing Properties of Two Dimensional Materials GeP_5 Enhanced after Annealing Treatment, *Appl. Phys. Lett.* **2019**, 114, 013103.

[31] Kronmüller H.; Parkin, S. *Handbook of Magnetism and Advanced Magnetic Materials: Volume 4: Novel Materials*; John Wiley & Sons, Inc.: West Sussex, UK, **2007**.

[32] Koledintseva, M. Y.; Dubroff, R. E.; Schwartz, R. W. A Maxwell Garnett Model for Mixtures Containing Conducting Particles at Optical Frequencies, *Prog. Electromagn. Res. PIER.* **2006**, 63, 223–242.

[33] Koledintseva, M.; Ravva, C.; Drewniak, J.; Rozanov, K.; Archambeault, B. Engineering of Composite Media for Shields at Microwave Frequencies, 2005 *International Symposium on Electromagnetic Compatibility*, **2005**, 1, 169–174.

[34] Sihvola, A. Mixing Rules with Complex Dielectric Coefficients, *P. Soc. Photo-Opt. Ins.* **2000**, 1, 393–415.

[35] Poudyal, N.; Rong, C. B.; Liu, J. P. Effects of Particle Size and Composition on Coercivity of Sm-Co Nanoparticles Prepared by Surfactant-Assisted Ball Milling, *J. Appl. Phys.* **2010**, 107, 8–11.

[36] Ravel, B.; Newville, M. ATHENA , ARTEMIS , HEPHAESTUS: Data Analysis for X-Ray Absorption Spectroscopy Using IFEFFIT, *J. Synchrotron Radiat.* **2005**, 12, 537–541.

[37] Newville, M. IFEFFIT: Interactive XAFS Analysis and FEFF Fitting, *J. Synchrotron Radiat.* **2001**, 8, 322-324.

[38] Tadić, M.; Spasojević, V.; Kusigerski, V.; Marković, D.; Remškar, M. Formation of ε-Fe_2O_3 Phase by the Heat Treatment of α-Fe_2O_3/SiO_2 nanocomposite, *Scr. Mater.* 58 **2008**, 58, 703–706.

[39] Gheiratmand, T.; Hosseini, H. R. M.; Davami, P.; Gjoka, M.; Song, M. The Effect of Mechanical Milling on the Soft Magnetic Properties of Amorphous FINEMET Alloy, *J. Magn. Magn. Mater.* **2015**, 381, 322–327.

[40] Raja, M. M.; Chattopadhyay, K.; Majumdar, B.; Narayanasamy, A. Structure and Soft Magnetic Properties of FINEMET Alloys, *J. Alloys Compd.* **2000**, 297, 199–205.

[41] Hernando, A.; Marín, P.; López, M.; Kulik, T.; Varga, L. K.; Hadjipanayis, G. Size Dependence of Coercivity in Nanostructured Soft Alloys, *Phys. Rev. B* **2004**, 69, 052501.

[42] Scherrer, V. P. Bestimmung der Inneren Struktur und der Größe von Kolloidteilchen Mittels Röntgenstrahlen, *Göttinger Nachrichten Math. Phys.* **1918**, 2, 98-100.

[43] Schäfer, R.; Hubert, A.; Herzer, G. Domain Observation on Nanocrystalline Material, *J. Appl. Phys.* **1991**, 69, 5325.

[44] Pradeep, K. G.; Herzer, G.; Choi, P.; Raabe, D. Atom Probe Tomography Study of Ultrahigh Nanocrystallization Rates in FeSiNbBCu Soft Magnetic Amorphous Alloys on Rapid Annealing, *Acta Mater.* **2014**, 68, 295–309.

[45] Li, C.; Yan, N.; Ye, Y.; Lv, Z.; He, X.; Huang, J.; Zhang, N. Thermal Analysis and Stability of Boron/Potassium Nitrate Pyrotechnic Composition at 180 ºC, *Appl. Sci.* **2019**, 9, 3630.

[46] Rubio-Zuazo, J.; Chainani, A.; Taguchi, M.; Malterre, D.; Serrano, A.; Castro, G. R. Electronic Structure of FeO, γ-Fe_2O_3,and Fe_3O_4 Epitaxial Films Using High-Energy Spectroscopies, *Phys. Rev. B* **2018**, 97, 1235148.

[47] López-Sánchez, J.; Muñoz-Noval, A.; Castellano, C.; Serrano, A.; del Campo, A.; Cabero, M.; Varela, M.; Abuín, M.; de la Figuera, J.; Marco, J. F.; Castro, G. R.; Rodríguez de la Fuente, O.; Carmona, N. Origin of the Magnetic Transition at 100 K in ε-Fe_2O_3 Nanoparticles Studied by X-Ray Absorption Fine Structure Spectroscopy, *J. Phys. Condens. Matter.* **2017**, 29, 485701

[48] López-Sánchez, J.; Serrano, A.; del Campo, A.; Abuín, M.; Salas-Colera, E.; Muñoz-Noval, A.; Castro, G. R.; de la Figuera, J.; Marco, J. F.; Marín, P.; Carmona, N.; Rodríguez de la Fuente, O. Self-Assembly of Iron Oxide Precursor Micelles Driven by Magnetic Stirring Time in Sol–Gel Coatings, *RSC Adv.* **2019**, 9, 17571–17580.

[49] López-Sánchez, J.; Muñoz-Noval, A.; Serrano, A.; Abuín, M.; de la Figuera, J.; Marco, J. F.; Pérez, L.; Carmona, N.; Rodríguez de la Fuente, O. Growth, Structure and Magnetism of ε-Fe_2O_3 in Nanoparticle Form, *RSC Adv.* **2016**, 6, 46380.

[50] Knobel, M.; Hernando, A.; Sánchez, M. L.; Marín, P.; Gómez-Polo, C.; Vázquez, M; Hernando, A. Influence of Nanocrystallization on the Magneto-Impedance Effect in FeCuNbSiB Amorphous Wires, *IEEE Trans. Magn.* **1995**, 31, 4009–4011.

[51] Alben, R.; Becker, J. J.; Chi, M. C. Random Anisotropy in Amorphous Ferromagnets, *J. Appl. Phys.* **2016**, 49, 1653.

[52] Paul, D. L. General Theory of the Coercive Force Due to Domain Wall Pinning, *J. Appl. Phys.* 53 **1982**, 53, 1649.

[53] Smart, J. S. The Néel Theory of Ferrimagnetism, *Am. J. Phys.* **1955**, 23, 356.

[54] Makhnovskiy, D. P.; Panina, L. V. Field Dependent Permittivity of Composite Materials Containing Ferromagnetic Wires, *J. Appl. Phys.* **2003**, 93, 4120–4129.

[55] Lagarkov, A. N.; Matytsin, S. M.; Rozanov, K. N.; Sarychev, A.K. Dielectric Properties of Fiber-Filled Composites, *J. Appl. Phys.* **1998**, 84, 3806–3814.

[56] Peng, H.-X.; Qin, F.; Phan, M.-H. *Ferromagnetic Microwire Composites*, Springer International Publishing, Mancheser, UK, **2016**.

[57] Lagarkov, A.; Sarychev, A. Electromagnetic Properties of Composites Containing Elongated Conducting Inclusions, *Phys. Rev. B - Condens. Matter Mater. Phys.* **1996**, 53, 6318–6336.

[58] Liu, Y.; Cui, T.; Wu, T.; Li, Y.; Tong, G. Excellent Microwave-Absorbing Properties of Elliptical Fe_3O_4 Nanorings Made by a Rapid Microwave-Assisted Hydrothermal Approach, *Nanotechnology*. **2016**, 27, 165707.

[59] Tong, G.; Liu, Y.; Cui, T.; Li, Y.; Zhao, Y.; Guan, J. Tunable Dielectric Properties and Excellent Microwave Absorbing Properties of Elliptical Fe_3O_4 Nanorings, *Appl. Phys. Lett.* **2016**, 108, 072905.

[60] Qiao, M.; Lei, X.; Ma, Y.; Tian, L.; He, X.; Su, K.; Zhang, Q. Application of Yolk–Shell Fe_3O_4@N-Doped Carbon Nanochains as Highly Effective Microwave-Absorption Material, *Nano Res.* **2018**, 11, 1500–1519.

[61] Hua, A.; Pan, D.; Li, Y.; Luan, J.; Wang, Y.; He, J.; Geng, D.; Liu, W.; Ma, S.; Zhang, Z. Fe_3Si-core/amorphous-C-shell nanocapsules with enhanced microwave absorption, *J. Magn. Magn. Mater.* **2019**, 471, 561–567.

[62] Savi, P.; Giorcelli, M.; Quaranta, S.; Multi-Walled Carbon Nanotubes Composites for Microwave Absorbing Applications, *Appl. Sci.* **2019**, 9, 1–10.

[63] Chung, D. D. L. Electromagnetic Interference Shielding Effectiveness of Carbon Materials, *Carbon*, **2001**, 39, 279–285.

[64] Li, L.; Chung, D. D. L. Electrically Conducting Powder Filled Polyimidesiloxane, *Composites*. **1991**, 22, 211–218.

[65] Qin, F.X.; Peng, H. X.; Pankratov, N.; Phan, M. H.; Panina, L. V.; Ipatov, M.; Zhukova, V.; Zhukov, A.; Gonzalez, J. Exceptional Electromagnetic Interference Shielding Properties of Ferromagnetic Microwires Enabled Polymer Composites, *J. Appl. Phys.* **2010**, 108, 044510.

[66] Liu, X.; Guo, H.; Xie, Q.; Luo, Q.; Sen Wang, L.; Peng, D. L. Enhanced Microwave Absorption Properties in GHz Range of Fe_3O_4/C Composite Materials, *J. Alloys Compd.* **2015**, 649, 537–543.

[67] Zhang, T.; Huang, D.; Yang, Y.; Kang, F.; Gu, J. Fe_3O_4/Carbon Composite Nanofiber Absorber with Enhanced Microwave Absorption Performance, *Mater. Sci. Eng. B*, **2013**, 178, 1–9.

[68] Hou, Y.; Zhang, Y.; Du, X.; Yang, Y.; Deng, C.; Yang, Z.; Zheng, L.; Cheng, L. Flexible Fe_3Si/SiC Ultrathin Hybrid Fiber Mats with Designable Microwave Absorption Performance, *RSC Adv.* **2018**, 8, 33574–33582.

[69] Zhang, M.; Li, Z.; Wang, T.; Ding, S.; Song, G.; Zhao, J.; Meng, A.; Yu, H.; Li, Q. Preparation and Electromagnetic Wave Absorption Performance of Fe_3Si/SiC@SiO_2 Nanocomposites, *Chem. Eng. J.* **2019**, 362, 619–627.

Graphical abstract